III-Nitride Intersubband Structures with Nonpolar Orientations

Third Annual Project Report

ECCS 1810318

Date Prepared: 07/20/21

1. Introduction

Gallium nitride (GaN/AlGaN) is a high-conduction-offset semiconductor system that has shown significant progresses in various applications within optoelectronics, photonics and power electronics. More recently, GaN heterostructures have attracted a great deal of attention for novel intersubband (ISB) devices to potentially encompass both infrared (IR) and terahertz (THz) spectrum. The large conduction band offsets, ultrafast electron relaxation times, and high longitudinal optical phonon energy (~92 meV) has made III-nitrides particularly unique for development of short-wavelength IR (λ = 1.4-3 μm) and THz wave (λ = 30-300 μm) ISB devices.

So far, most of the reported GaN intersubband structures have been on polar {0001} family of *c*-plane. Despite the great promises of nitrides for ISB devices, the conventional *c*-plane GaN features a large polarization field that reduces the transitions oscillator strength. In addition, the energy levels for the bound states in the multi-quantum-wells (MQWs) are very sensitive to the large electric fields in the heterostructures, which vary with strain. Growing the heterostructures on the nonpolar GaN, in contrast, would potentially overcome the issues with the conventional polar *c*-plane.

This project aims to develop a nonlinear metasurfaces and THz emitters based on the *m*-plane and *a*-plane GaN/AlGaN heterostructures grown on high-quality free-standing GaN substrates and r-plane sapphire substrates The *r*-plane sapphire substrate provides a large area inexpensive substrate alternative to small and expensive free-standing non-polar GaN substrates. However, GaN/AlGaN heterostructure growth on r-plane sapphire results in high defect densities and it is unclear how these defects may affect intersubband transitions. based on these non-polar planes. These discoveries will greatly enrich the developments of applications of GaN material in related realms.

In the year 3 of the project, we focused on investigating the performance of GaN/AlGaN heterostructures grown on r-plane sapphire and on developing the first GaN/AlGaN nonlinear metasurfaces for SHG in the 3-4 microns wavelength range.

2. ISB transitions in MQWs grown on r-plane sapphire

(a) MQW designs and growth sheet

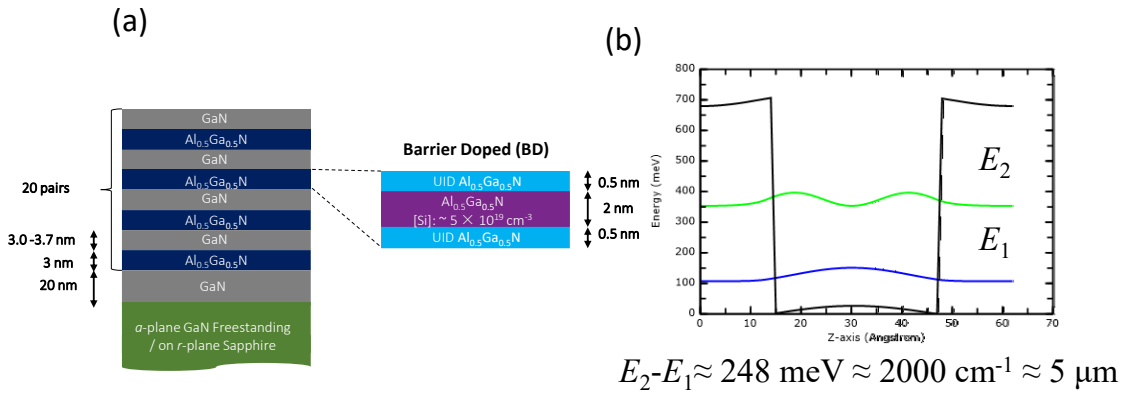

Fig. 1: MQW designs of the single ISB transition samples of different substrates (*a*-plane freestanding GaN and *r*-plane sapphire). **(a)** Cross-sectional schematics of nonpolar *m*-plane and *a*-plane 20 pairs of GaN/$Al_{0.5}Ga_{0.5}N$ ISB heterostructures with fixed AlGaN quantum barrier (QB) thickness (3.0 nm) and different GaN quantum well (QW) thicknesses (3.0, 3.3, and 3.7 nm). Doping profile are shown in the right panel of Fig (a). The nominal Silicon (Si) doping concentration for the sample are 5×10^{19} cm^{-3} and uniformly distributed in the middle 2 nm barrier area. The sample substrates have two type: *a*-plane freestanding GaN and *r*-plane sapphire. **(b)** Calculated conduction band diagram and squares of electron wave functions for the ground and the first excited states for a 3.3 nm-wide BD GaN/$Al_{0.5}Ga_{0.5}N$ QW structure. The 1-to-2 ISB transition energies, wavenumber and wavelength are about 248 meV, 2000 cm^{-1} and 5 µm, respectively.

In order to investigate the impact of extended defects on the ISB transactions in MQWs grown on r-sapphire substrates. Identical 20 pair *a*-plane MQW heterostructures have been designed, grown and measured both on *a*-plane freestanding GaN and *r*-plane sapphire, which are denoted as *a*-GaN-FS and *a*-GaN/*r*-Sap. Schematic of the heterostructures designs are shown in Fig. 1 and further details are provided in Table 1.

The ISB structures were then grown on co-loaded *a*-GaN-FS and *a*-GaN/*r*-Sap substrates. The structures consisted of 20 periods of nominal GaN/$Al_{0.4}Ga_{0.4}N$ MQW heterostructures on a 20 nm unintentionally doped (UID) GaN buffer layer. Three different sets of structures were grown, for which the thickness of GaN quantum wells (QWs) were varying. For all the structures, the thicknesses of the AlGaN quantum barriers (QBs) were kept constant at 3.0 nm. Out of the 3

nm QBs, the bottom and top 0.5 nm of the QBs were kept UID, while the innermost 2.0 nm of the AlGaN QBs were doped with Si (up to ~ 5×10^{19} cm^{-3}) to provide enough modulation doping to enhance carrier concentration in the active QWs.

Crystal orientation	Substrate	QW thickness (nm)	Configuration (nm)
a-plane	*a*-plane GaN	3.0	**1*/0.5**/3.0/**0.5/1***
		3.3	**1*/0.5**/3.3/**0.5/1***
		3.7	**1*/0.5**/3.7/**0.5/1***
	r-plane Sapphire	3.0	**1*/0.5**/3.0/**0.5/1***
		3.3	**1*/0.5**/3.3/**0.5/1***
		3.7	**1*/0.5**/3.7/**0.5/1***

Table 1: Wafer growth sheet for GaN single ISB samples of different substrates (*a*-plane freestanding GaN and *r*-plane sapphire). There are 3 quantum well thickness for each substrate: 3.0, 3.3 and 3.7 nm. The configuration column shows the single QW stage for each samples. The actual MQW active region composes of 20 pair of these stage. The bold is $Al_{0.5}Ga_{0.5}N$ barrier and plain is GaN well. The asterisks (*) mean which layers Si atoms were doping with uniform volume nominal concentrations of 5×10^{19} cm^{-3} .

For each substrate, three different samples with 3.0, 3.3 and 3.7 nm nominal well widths were grown to ensure the resonance frequency to locate in the observable range of the Fourier-transform infrared spectrometer in our laboratory.

(b) Heterostructure growth and structural characterization

The structures were all grown by the Veeco Gen 930 NH_3 molecular beam epitaxy (MBE), where NH_3 decomposition at elevated temperatures provide elemental N for growth of GaN and its alloys. In the NH_3-MBE system, Ga, Al effusion cells were used to provide metallic elements and Si effusion cell for Si *n*-type dopant. Two sets of samples were considered. The

first set of samples use *a*-GaN freestanding (*a*-GaN-FS) from Mitsubishi Chemical Corporation (MCC) with no basal-plane stacking faults (BSFs), prismatic stacking faults (PSFs), and partial dislocation (PDs), and a threading dislocation (TD) density of ~ 10^5 cm^{-2}. The second set of samples utilized heteroepitaxial *a*-plane GaN templates grown on *r*-plane sapphire (*a*-GaN/*r*-Sap) (the most commonly used substrate for the growth of nonpolar GaN). The heteroepitaxy of *a*-GaN/*r*-Sap templates were carried out by metal-organic chemical vapor deposition system (MOCVD) in a close-coupled showerhead reactor using trimethylgallium (TMG) and NH_3 as precursors and hydrogen (H_2) as the main carrier gas. 2 μm-thick *a*-plane GaN templates were grown on *r*-plane sapphire. The epitaxial process began with sapphire nitridation at 1120°C and a low temperature GaN buffer deposition at 690°C at 100 Torr, followed by buffer annealing and 3D crystal formation at 1200°C and 700 Torr and crystal expansion at 1090°C and 300 Torr before the final coalescence step at 1200°C and 10 Torr.

The microstructure of nonpolar heteroepitaxial films is very different from those deposited along the polar *c*-direction, which is dominated by the presence of vertically threading perfect dislocations mainly of *a*-type (edge) and *a* + *c* type (mixed). Even though the densities and nature of extended defects in heteroepitaxial nonpolar GaN may be a bit different depending on the substrates, similar general trends are observed for nonpolar *a*-GaN/*r*-Sap layers. Figure 2(a) shows a high-resolution cross-sectional STEM image of the *a*-GaN grown on *r*-sapphire by MOCVD, indicating the different types of defects. The cross-sectional images clearly show extensive TDs, BSFs terminated by PDs, and PSFs. The densities of the different defects in these samples are ≈ 4×10^5–10^6 cm^{-1} for BSFs, ≈ 9×10^{10} to 2×10^{11} cm^{-2} for PDs and ≈ 5×10^3 to 2×10^4 cm^{-1} for PSFs. The surface morphology of *a*-GaN/*r*-Sap is also shown in Figure 2(b), indicating a typical elongated comet-like features along *c*-directions. The diagonal lines along the atomic force microscopy (AFM) images are along the +*c* [0001] direction and at 90 degrees the *m*-direction $[10\bar{1}0]$

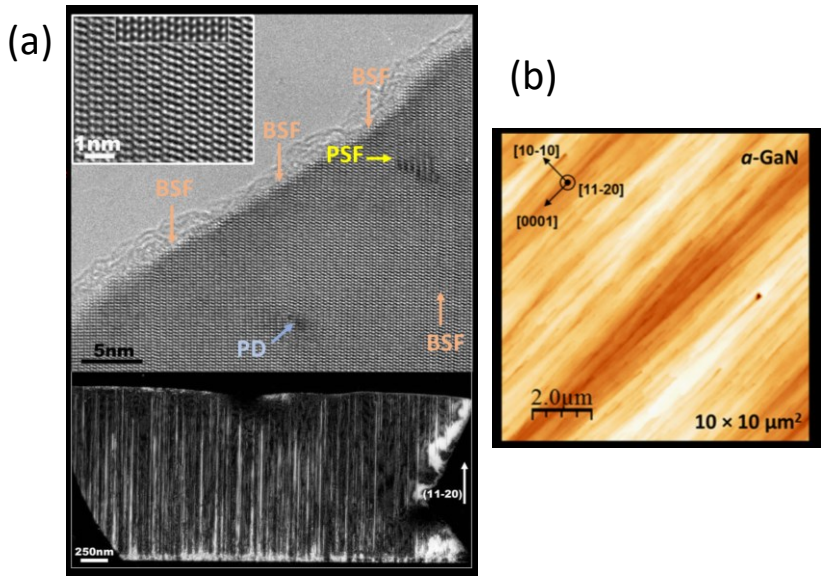

Fig. 2: **(a)** Plan-view (top) high-resolution scanning transmission electron microscopy (STEM) image of the *a*-GaN/*r*-Sap template along the $[1\bar{1}20]$ zone axis, showing the dominant defects are basal-plane stacking faults (BSFs) which are indicated by orange arrows. BSFs may either be terminated by partial dislocation (PDs) (pale blue arrows), or two neighboring BSFs may be connected by a $(1\bar{1}20)$ PSF (yellow arrow). Bottom of Fig (a) shows a cross sectional image of PDs which are vertically threading from the interface to the surface. **(b)** Representative surface of *a*-plane orientation of GaN indicating elongated features toward *c*-direction.

The structures were then characterized using high-resolution x-ray diffraction HRXRD, STEM, AFM, and APT. To evaluate the interface quality, the QW thicknesses, and characterization of the extended defects, a HAADF-STEM was used. The STEM samples were prepared by FIB with a FEI Helios Dualbeam Nanolab 600 instrument. A ThermoFisher Talos G2 200X TEM/STEMw/ChemiSTEM EDS system operating at 200 kV was used to perform the microstructure and chemical element mapping. APT was also used to investigate the compositions and alloy distribution in the GaN/AlGaN heterostructures in 3D at the nanometer scale. The needle shaped specialized APT samples were prepared using an FEI Helios 600 dual beam FIB instrument and the analysis was performed in laser-pulse mode using a Cameca 3000X HR Local Electrode Atom Probe (LEAP).

Figure 3 shows the structural defects in GaN/AlGaN MQWs grown on *a*-GaN/*r*-Sap in the cross-section along $[10\bar{1}0]$ direction using two-beam bright field (BF) diffraction

contrast (Fig. 3 (a, c, e)) and weak beam dark field (DF) diffraction contrast (Fig. 3 (b, d). The results indicate all dislocations are located in the *c*-plane. Comparison of the STEM images taken in $g = 000\bar{2}$ electron diffraction condition (Fig. 3 (a, b)), in which *a*+*c*-type dislocations are visible, while pure *a*-type dislocations are invisible) and those taken in $g = \bar{1}\,\bar{1}20$ electron diffraction condition, in which both *a*-type and *a*+*c*-type dislocations are visible, ~ 80% of the dislocations are concluded to be of *a*-type and only ~ 20% of *a*+*c* type. High density of BSFs can be observed in the image obtained by tilting the sample by ~ 30° to find the $g = 01\bar{1}0$ diffraction condition (Fig. 3 (e)).

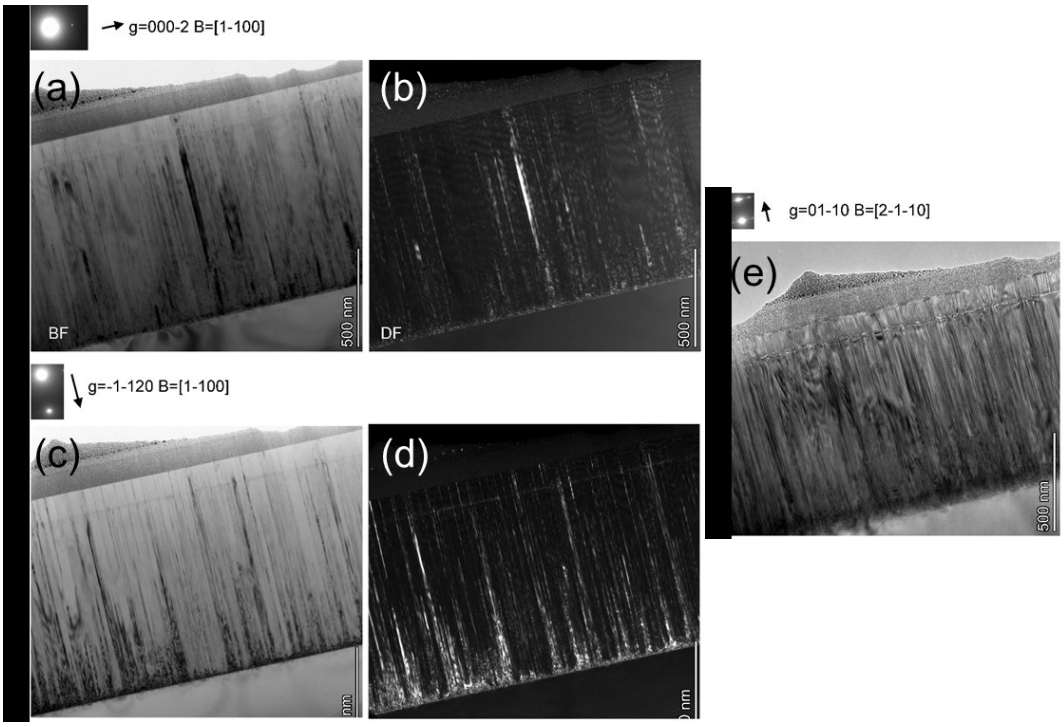

Fig. 3: Cross sectional using high-resolution x-ray diffraction images of a GaN/AlGaN MQW structures on *a*-GaN/*r*-Sap with **(a, c, e)** two-beam bright field (BF) diffraction contrast and **(b, d)** weak beam dark field (DF) diffraction contrast along (a, b) $g = 000\bar{2}$, (c, d) $g = \bar{1}\,\bar{1}20$, and (e) $g = 01\bar{1}0$

Figure 4 compares the structural properties of the epilayers grown on *a*-GaN-FS and on *a*-GaN/*r*-Sap using high-resolution XRD ω-2θ scans and cross-sectional STEM. XRD data indicates sharp GaN peaks for the samples on *a*-GaN-FS (Figure 4 (a)), while much weaker GaN

peaks are observed for all the structures grown on *a*-GaN/*r*-Sap (two to three orders of magnitude less in peak intensity) (Fig. 4 (b)). The MQW structures grown on *a*-GaN-FS also show more pronounced satellite (SL) peaks (five intense SL peaks) as shown in Fig. 4 (a) which are normally observed for short-period superlattices. In contrast, the structures grown on *a*-GaN/*r*-Sap only show four less pronounced SL peaks, as shown in Fig. 4 (b). These results are indicative of higher interface abruptness for the structures grown on *a*-GaN-FS. The period of the SL peaks consistently reduces for thicker QW structures for both cases, consistent with larger periodicity of the superlattice structure. Cross-sectional HAADF-STEM (Fig. 4 (c, d)) image comparison of selected samples from the superlattices with 3.0 nm QW width indicate a large difference in the densities of defects extended to the MQW heterostructures between the two structures, as expected from their extremely different substrate qualities.

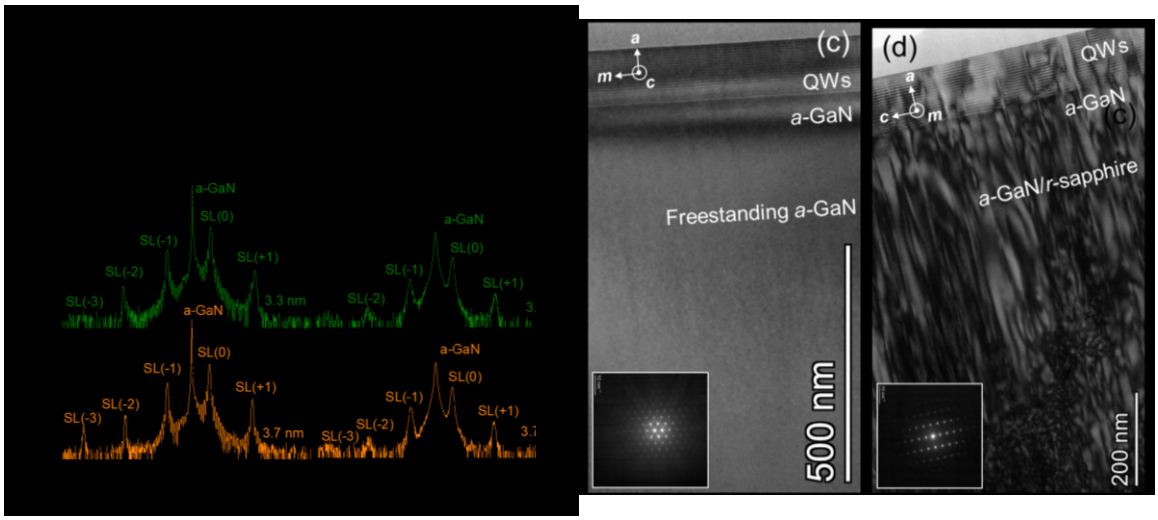

Fig. 4: **(a, b)** HRXRD ω-2θ scans and **(c, d)** cross-sectional HAADF-STEM images of the structures on (a, c) *a*-GaN-FS and (b, d) *a*-GaN/*r*-Sap.

The ISB optical transition properties, such as linewidths, can be strongly dependent on the interface abruptness. Hence, the interface quality and surface morphology of the structures for 3.0 nm QW width grown on *a*-GaN-FS and *a*-GaN/*r*-Sap were compared using cross-sectional STEM/EDS (Fig. 5) and AFM (Fig. 6). The structure grown on *a*-GaN-FS show a

higher interface quality compared to the *a*-GaN/r-Sap sample. Also, the thickness of the QWs are slightly smaller for *a*-GaN-FS (~ 2.9-3.0 nm) compared to *a*-GaN/*r*-Sap (~ 3.1 to 3.2 nm) samples. The AFM results (Fig. 6) also indicate a larger room-mean-square (RMS) roughness values for the *a*-GaN/*r*-Sap substrates (1.86 nm for 2×2 μm^2 scans) compared to the *a*-GaN-FS substrate (0.16 nm) and the corresponding ISB structure on *a*-GaN/*r*-Sap (2.3 nm) compared to the one grown on *a*-GaN-FS (0.3 nm).

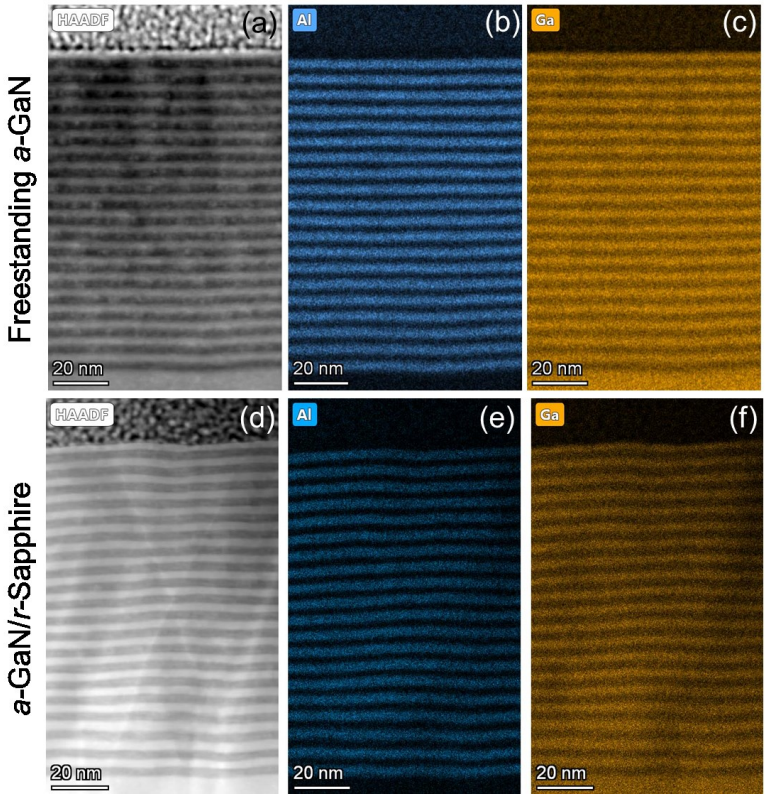

Fig. 5: **(a, d)** HAADF STEM images and corresponding **(b, e)** Al and **(c, f)** Ga elemental maps of GaN/AlGaN MQW heterostructures with 3.0 nm QWs grown by NH_3-MBE on (a, b, c) *a*-GaN-FS and (d, e, f) *a*-GaN/*r*-Sap substrates.

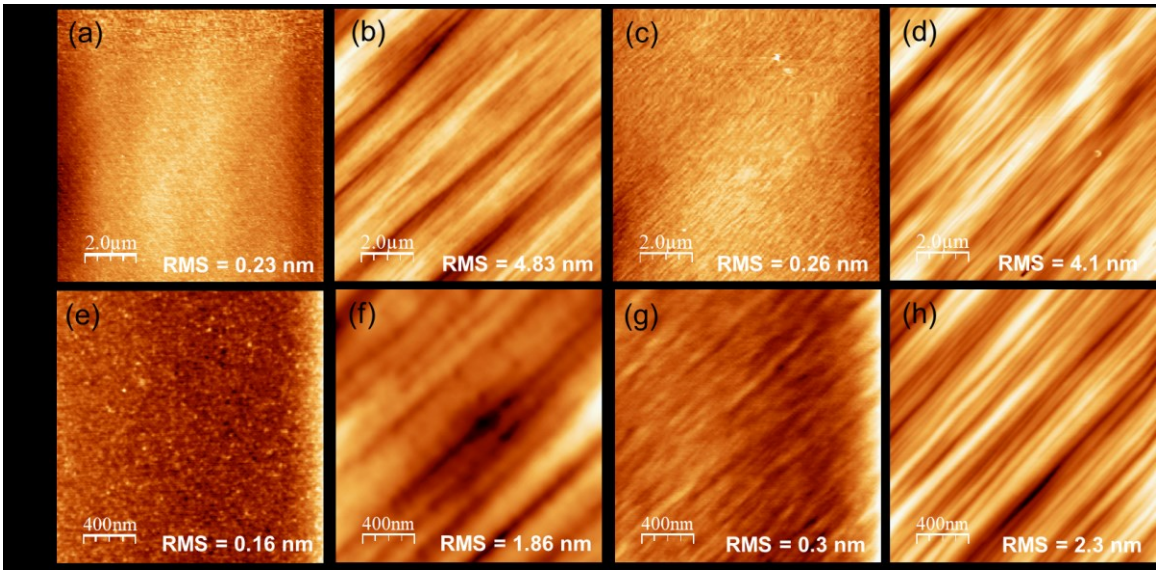

Fig. 6: **(a, b, c, d)** 10×10 μm^2 and **(e, f, g, h)** 2×2 μm^2 AFM scans of (a, e) *a*-GaN-FS and (b, f) *a*-GaN/*r*-Sap substrates as well as ISB GaN/AlGaN MQWs grown on (c, g) *a*-GaN-FS and on (d, h) *a*-GaN/*r*-Sap.

Figure 7 compares APT data and analysis of MQW samples with 3.0 nm QWs grown on *a*-GaN/*r*-Sap and *a*-GaN-FS substrates. According to the APT data, along the growth direction, the top interfaces between GaN and AlGaN (QW/QB interfaces) are slightly more abrupt than the bottom interfaces (Fig. 7), similar to our previous observations on other GaN/AlGaN MQW structures. As shown in the variations of Ga/Al+Ga and Al/Al+Ga profiles along the growth directions (Fig. 7 (b, f)), the Al fraction in the AlGaN layers varies in the range 38-45% with ~ 8% deviation for the structure grown on *a*-GaN/*r*-Sap and in the range 38-40% with ~ 4% deviation for the structure grown on *a*-GaN-FS. A normal Gaussian distribution of the Al atoms in the AlGaN QBs for the structure grown on *a*-GaN-FS (Fig. 7 (h)) indicates a natural random alloy disorder without significant clustering with an average composition of ~ 40%. For the structure grown on *a*-Ga/*r*-Sap, however, the distribution of the Al atoms is not as symmetric and does not fully obey a Gaussian model (Fig. 7 (d)), which indicates alloy clustering to some degree, while maintaining a similar average composition ~30% as that of the structure on *a*-GaN-FS.

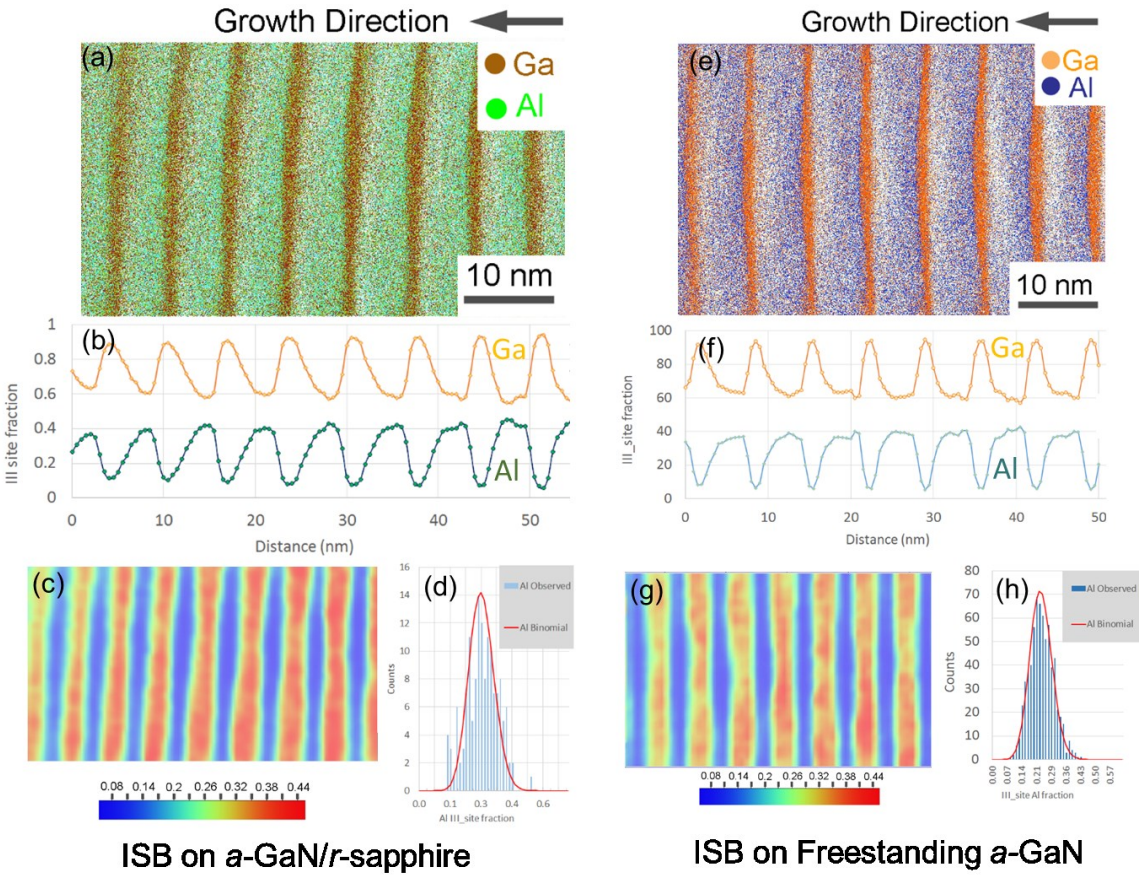

Fig. 7: **(a, e)** APT data and analysis, **(b, f)** atomic line profiles of Ga and Al concentrations, **(c, g)** Al composition maps along the growth direction, and **(d, h)** distribution of the Al contents in the AlGaN QBs for the ISB structures containing a 20-period nonpolar *a*-plane GaN/AlGaN MQW heterostructures on (a, b, c, d) *a*-GaN/*r*-sapphire and (e, f, g, h) freestanding *a*-GaN.

(c) Intersubband absorption measurements

ISB optical absorption spectra of the samples were then measured using an FTIR transmission setup discussed in the previous report.. The ISB absorption spectra for *a*-GaN/*r*-Sap and *a*-GaN-FS structures are shown in Fig. 8.

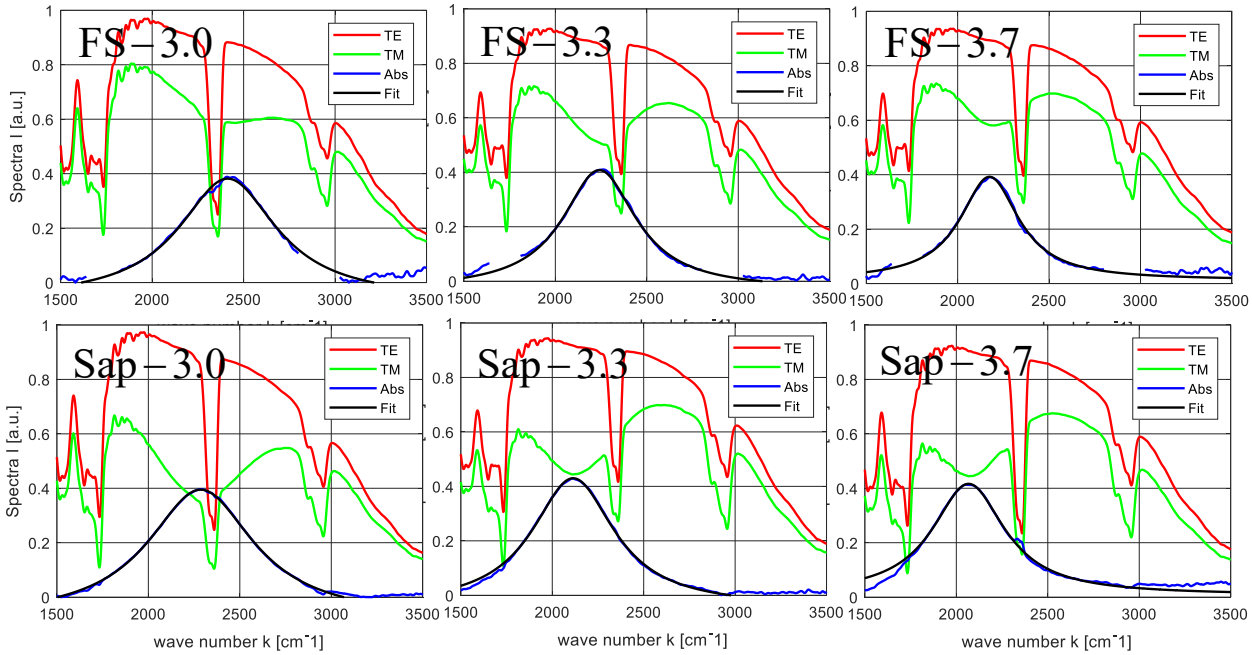

Fig. 8: Experimental spectra of single ISB sample of different substrates (*a*-plane freestanding GaN, labelled "FS" and *r*-plane sapphire, labelled "Sap") and different quantum well thickness (3.0, 3.3, 3.7 nm). The green and red lines: the TE and TM intensity spectra were received by the MCT. The blue and black lines: the calculated absorption spectrum and their Lorentz fitting.

QW thickness	***a*-GaN-FS (Lorentz fitting)**				***a*-GaN/*r*-Sap (Lorentz fitting)**			
	$1/\lambda_{12}$ (cm^{-1})	E_{12} (meV)	$2\gamma_{12}$ (cm^{-1})	$2\gamma_{12}$ meV)	$1/\lambda_{12}$ (cm^{-1})	E_{12} (meV)	$2\gamma_{12}$ (cm^{-1})	$2\gamma_{12}$ (meV)
3.0 nm	2413	299.1	650.6	80.7	2286	283.5	704.7	87.4
3.3 nm	2241	277.8	489.2	60.7	2114	262.1	546.0	67.7
3.7 nm	2174	269.6	390.6	48.4	2067	256.2	480.6	59.6

Table 2: Peak energy E_{12} and linewidth $2\gamma_{12}$ comparison of all heterostructures in Table 1 and Fig. 8. "*a*-GaN-FS" represents the *a*-plane GaN MQW structure grown on *a*-plane GaN freestanding substrate and "*a*-GaN/*r*-Sap" represents the *a*-plane GaN MQW structure grown on *r*-plane sapphire substrate. The corresponding wavenumber, which are directly observed in experiment, are also listed. The values are extracted from the Lorentz fitting of experimental post-proceed data in Fig. 8.

The summary of the measured transition energies and linewidths is listed in Table 2. All the structures show a clear decrease of the ISB absorption peak energy with increasing QW

width as expected from quantum-mechanical calculations. All *a*-GaN/*r*-Sap show slightly broad peaks than the corresponding *a*-GaN-FS structures. The average linewidths of *a*-GaN-FS structures are 63.3 meV. Same structure with low doping concentration have an average linewidths of 66.6 meV (listed in Table 2) No significant difference in ISB linewidths was observed between different doping concentration for barrier doped samples. However, the linewidths changing range is wider for the high doping concentration, which is due to the stronger many-body effects

(d) Key results

For a given QW width, the co-loaded ISB structures grown on *a*-GaN/*r*-Sap show lower ISB transition energies than those grown on freestanding *a*-GaN-FS, which may be attributed to slightly thicker QWs for the structures grown on *a*-GaN/*r*-Sap, as indicated in STEM results. The slight difference in growth rate could be due to the difference in the surface and bulk properties of the highly defective substrates compared to the high-quality freestanding GaN. The ISB structures grown on *a*-GaN/*r*-Sap also shows a 10-20% larger absorption linewidths compared to those grown on a-GaN-FS. However, despite the nearly 5 orders of magnitude difference in the defect densities for the two sample sets, the ISB absorption linewidth is not significantly different between the samples grown on the two different substrates. Therefore, the data suggests that unlike band-to-band transition devices, the ISB absorption is more tolerant to extended defects. We note that these findings are consistent with the recent results obtained for intersubband devices with As- and Sb-heterostructures grown foreign substrates **Error! Reference source not found.**. The larger ISB absorption linewidths for the structures grown on a-GaN/r-Sap can be partially explained by the surface morphology and interface quality differences. A systematic optimization of the growth conditions can improve the surface morphology of the a-GaN/r-Sap templates to further improve the interface quality and the ISB absorption properties. Given the manufacturing challenges of high-quality nonpolar GaN substrates, the low sensitivity of the ISB properties to the extended defects may provide a cost-effective and scalable approach for

producing efficient ISB emitters in the mid- to far-IR using heteroepitaxial nonpolar III-nitride system on Sapphire and Si.

Co-loaded structures grown on freestanding *a*-plane with no BSFs, PSFs, and PDs, with low TD densities of ~ 10^5 cm^{-2} were compared with those grown on *a*-GaN templates on *r*-sapphire with BSF, PSF, PD and TD densities of ~ 4×10^5 to 10^6 cm^{-2}, 5×10^3 to 2×10^4 cm^{-2}, ~ 9×10^{10} to 2×10^{11} cm^{-2} and ~ 10^{10} cm^{-2}, respectively. The results indicate that over 5 orders of magnitude difference in densities of extended defects did not have significant impact on the transition energy and linewidth of the ISB absorption. The strong defect tolerance in the nonpolar *a*-plane ISB structures can be due to the nature of defects and their energy levels with respect to the conduction band minima, which is not affecting ISB properties. Our results can pave the way toward low-cost scalable nonpolar III-nitrides for room temperature QCLs and optical frequency conversion using optical metasurfaces for mid- to far-IR applications.

These results have been submitted for publication in June 2021 [1].

3. GaN SHG metasurfaces

(a) QW designs and growth sheet

Following initial demonstration of high-quality ISB transitions in a single QW GaN/AlGaN heterostructure in year 2, we proceed to design more advanced GaN/AlGaN heterostructures based on multiple ISB transitions in coupled quantum wells. Such a heterostructure ideally requires three levels which have equal energy level differences. In order to demonstrate the possible SHG application of GaN-based heterostructure, a three-level MQW was designed. Figure 9(a) schematically shows the detailed ISB structures grown for this investigation. The band diagram of this MQW is shown in Fig. 9(b). The configuration is

1.5/3.3/**0.4**/1.2/**1.5,** (**$Al_{0.5}Ga_{0.5}N$**/GaN) in nm; the first and last 15 nm QBs were doped by Si of the concentration 2.6×10^{19} cm^{-3}, which make Fermi level just below E_2 by 2.66 kT, where k is Boltzmann constant (= 1.38064852 × 10^{-23} J/K) and T is room temperature (≈ 300K). The designed SHG wavelength is from 8 μm to 4 μm with E_{12} and E_{23} equal to 153.65 and 149.43 meV, respectively.

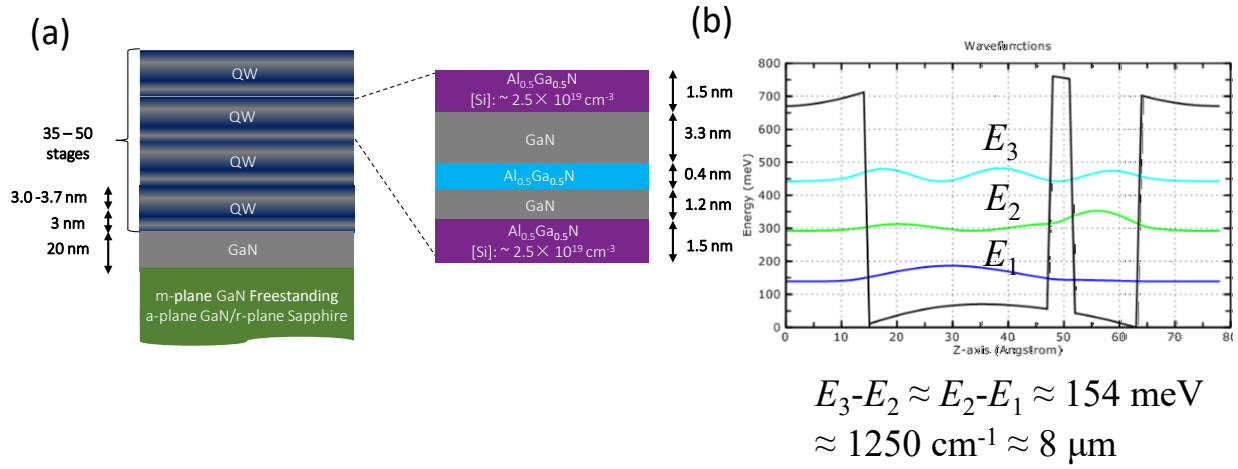

Fig. 9: MQW design of the SHG samples of different wafer types (*m*-plane freestanding GaN, labelled "*m*-FS", and *a*-plane GaN grown on *r*-plane sapphire, labelled "*a*-Sap"). **(a)** Cross-sectional schematics of SHG MQW heterostructures with doping profile are shown in the right panel of Fig (a). The nominal Si doping concentration for the sample is 2.6×10^{19} cm^{-3} and uniformly distributed in the two outer QBs. **(b)** Calculated conduction band diagram and squares of electron wave functions for first three states for GaN MQW heterostructures. The designed SHG wavelength is from 8 μm to 4 μm with E_{12} and E_{23} equal to 153.65 and 149.43 meV.

Based on the discussions in the previous section we can use the *a*-GaN/r-Sap as the alternative for *a*-GaN-FS with no significant performance drops for ISB transition applications. We used the *a*-GaN/r-Sap, denoted as "*r*-Sap", along with the *m*-plane freestanding GaN, denoted as "*m*-FS" to grow the SHG samples.

Active region period number (total thickness)	Wafer type	Surface cracks	configuration (nm)
35 (280 nm)	*m*-FS	No	**15***/33/**4**/12/**15***
	r-Sap	No	**15***/33/**4**/12/**15***
50 (400 nm)	*m*-FS	Yes	**15***/33/**4**/12/**15***
	r-Sap	Yes	**15***/33/**4**/12/**15***

Table 3: Wafer growth sheet for SHG samples of different wafer types (*m*-plane freestanding GaN, labelled "*m*-FS", and *a*-plane GaN grown on *r*-plane sapphire, labelled "*a*-Sap") and MQW stage numbers (35 and 50 stages, which are corresponding to 280 nm and 400nm total MQW thickness). The "surface cracks" column indicates whether there are visible cracks in the sample surfaces after the MQWs growths. The configuration column shows the single QW stage for each samples, which is identical. The actual MQWs compose of multiple these QW stage (35 or 50). The bold is $Al_{0.5}Ga_{0.5}N$ barrier and plain is GaN well. The asterisks (*) mean which layers Si atoms were doping with uniform volume nominal concentrations of 2.6×10^{19} cm^{-3} .

Two different numbers of MQW stages are used: 35 and 50 stages, which are corresponding to 280 nm and 400nm total MQW thicknesses. Table 3 shows the wafer growth sheet for the SHG samples of different wafer types and MQW stage numbers

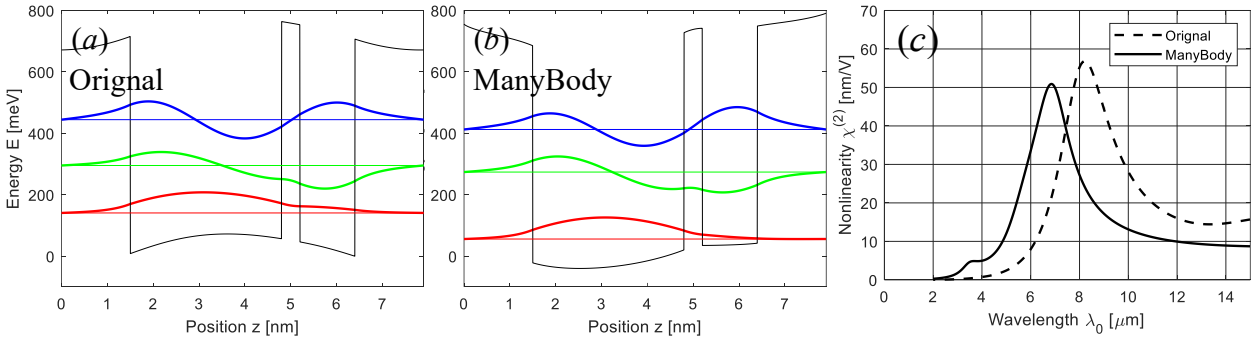

Fig. 10: Band diagram of SHG samples without **(a)** and with **(b)** many-body effects. **(c)** Expected nonlinearity as a function of input wavelength of such SHG sample without (dash line) and with (solid line) many-body effects. Note: except energy levels, the dipole moments z_{ij} in nonlinearity, is also affected by many-body effects

The nonlinearity, which is described the second order susceptibility, $\chi_{zzz}^{(2)}$ as a function incident light frequency ω were calculated by Eq. (1):

$$\chi_{zzz}^{(2)}(\omega) \approx \frac{ne^3}{\hbar^2 \varepsilon_0} \frac{z_{12} z_{23} z_{13}}{(\omega - \omega_{12} + i\gamma_{12})(2\omega - \omega_{13} + i\gamma_{13})} \quad (1)$$

In the calculation, 600 cm^{-1} or equivalent 74.4 meV was used to estimate linewidths $2\gamma_{12}$ and $2\gamma_{13}$ of ISB transactions. This value is the average of the linewidths measured from the experiments (shown in Table 2)

We found that the results obtained with Eq. (1) are quite different whether we considere many-body effects in our bandstructure calculations or not. The maximum nonlinearity, $\max\left|\chi_{zzz}^{(2)}\right|$ is 56.9 nm/V at 8 μm without many-body effects while the maximum nonlinearity, $\max\left|\chi_{zzz}^{(2)}\right|$ is 50.8 nm/V at 6.5 μm with the many-body effects.

The samples were grown also by the Veeco Gen 930 ammonia molecular-beam epitaxy (NH_3-MBE) as in the previous section. We found that there are some visible cracks on the 50 stage (400 nm) samples. The cracks may be due to the internal tense in the thicker MQW structures.

(b) Absorption measurements results

The absorption spectra of the SHG samples of different stage numbers, 35 stages (280 nm MQW) and 50 stages (400 nm MQW) are shown in Fig. 11 (a,b). For the comparison, we include the theoretically calculated imaginary parts of perpendicular component of MQW permittivity, $\mathrm{Im}\{\varepsilon_\perp\}$ in Fig. 11(c). As follows from the comparison, the 1-2 transition in the measured samples occur approximately at the design wavelength and has the expected linewidth. In contrast the 1-3 transition visible in the theoretical simulations in Fig. 11(c) cannot be observed in the experimental spectra in Fig. 11(a,b). This may be due to several reasons related to either the growth quality (interwell barrier is of a different thickness than intended), due to higher-than expected spectral linewidth of the diagonal 1-3 transition, or due to calculations (i.e. many body effects are not properly included). To find the reasons for this discrepancy and to produce MQW

heterostructures that have all 3 energy levels optically coupled at the right frequencies for the maximum optical nonlinearity, further simulations, heterostructure growths and testing will be performed in the year 4 of the project (operating under a no-cost extension).

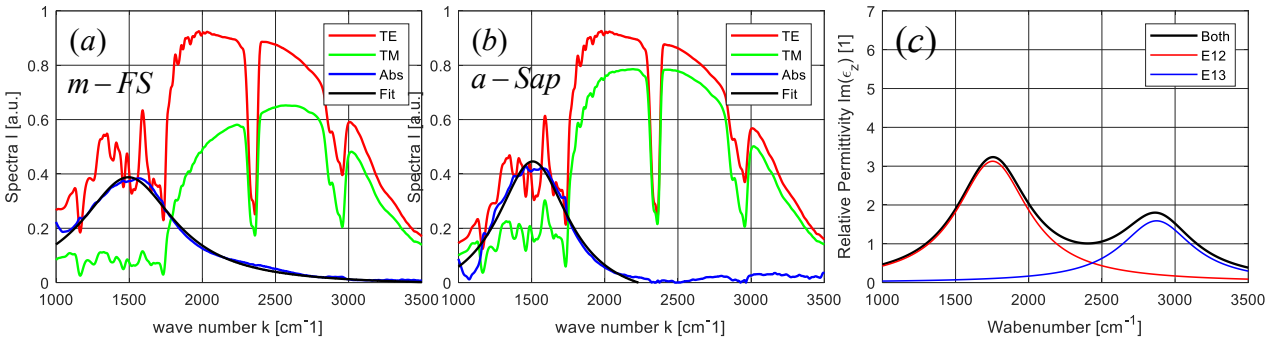

Fig. 11: Experimental spectra of 35 stages SHG sample of **(a)** *m*-plane freestanding GaN and **(b)** *a*-plane GaN on *r*-plane sapphire. The green and red lines: the TE and TM intensity spectra were received by the MCT. The blue and black lines: the calculated absorption spectrum and their Lorentz fitting. **(c)** Calculated absorption spectra (imaginary part of relative permitted versus wavenumber), in which each transaction is considered separately (red line for 1-to-2 ISB transition, and blue line for 1-to-3 ISB transition) and then collectively (black line)

(c) Incomplete back plane metasurface

In preparation for the future processing of GaN/AlGaN heterostructures into nonlinear metasurfaces, we performed design, simulation and processing of metasurface nanoresonators using the SHG MQW sample discussed in Figs. 10-11. To couple light along the growth direction of MQW for SHG, a metal antenna array metasurface as proposed as the T-shape structure shown in Fig. 12 This structure forms a quasi-nanocavity beneath the top antenna because the metal back plane is incomplete. The design is similar to the one successfully used in our group recently for InGaAs/AlInAs heterostructures at longer wavelengths [2]. The lengths of two arms of T-shape antenna have been designed to resonate at fundament frequency in *x*-axis and second harmonic frequency in *y*-axis.

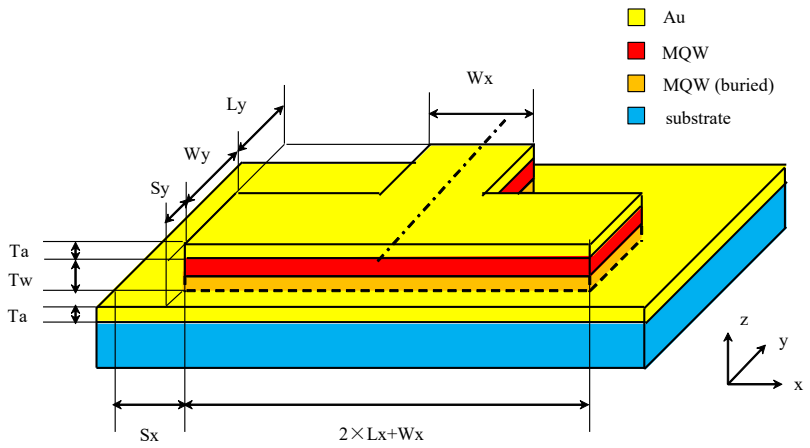

Fig. 12: Schematic drawing of unit cell design of incomplete back plane GaN SHG metasurface. Some part of MQW is buried in the ground gold layer. The substrate is GaN for *m*-FS sample and *r*-plane sapphire for *a*-Sap sample. There are several dimension sizes used to maximize the overlaps integrals *I* in the simulations: long arm length L_x, long arm width W_x, short arm length L_y, short arm width W_y, half spacing in *x*-axis S_x, half spacing in *y*-axis S_y, and the antenna metallization thickness T_a. T_a is set to 50 nm in order to avoid the side-wall metal deposition issue.

Assuming the incident light polarized along *x*-axis and SHG light polarized along *y*-axis, the *yxx* component of the effective susceptibility $\chi^{(2)}_{eff,yxx}$ of normal reflected SHG can be calculated by Eq. (2) as discussed in Ref. [3]:

$$\chi^{(2)}_{eff,yxx} = \chi^{(2)}_{QW} \frac{\int_{QW} E_{SH,z} E_{p,z} E_{p,z} \mathrm{d}v}{\left|E_{SH,y}\right| \left|E_{p,x}\right|^2 V_{QW}} = \chi^{(2)}_{QW} I \tag{2}$$

where $\chi^{(2)}_{QW}$ is intersubband nonlinear susceptibility of the MQWs shown in Eq. (1), $\vec{E}_{p,x}$ is incident pump field, $\vec{E}_{SH,y}$ is second-harmonic field, $E_{SH,z}$ and $E_{p,z}$ are the *z*-components of the pump and SH fields, and V_{QW} is the volume of the MQWs in the single nanoresonator. This overlap integral *I* relies on nearfields and depends on the dimensions of nanocavity structure.

CST simulations based on finite element method (FEM) have been used to estimate near-fields and optimize the overlaps integrals *I*. based on the simulations, the optimal overlaps integrals *I* are 0.5599 and 0.7213 for the 280 and 400 nm thick MQW respectively. The optimal dimension sizes and simulated reflectance $|S_{11}|$ (defined as E_{SH}/E_{inc}) of single nanoresonator of the incomplete back plane GaN SHG metasurface are listed in Table 3 and Fig. 13.

Incomplete backplane		L_x	L_y	W_x	W_y	S_x	S_y
T_w=400	designed	578.20	264.69	448.29	200.00	50.00	173.17
T_w=280	designed	526.40	231.89	443.00	200.00	50.00	169.95
	fabricated	516.9	235.90	452.20	208.40	49.15	172.30
	Errors	1.80%	1.73%	2.08%	4.2%	1.70%	1.37%

Table 3: Optimal dimension sizes in nm (see Fig. 12) based on the CST simulation to have the maximum overlap integral I (defined in Eq. (2)). The width of long-arm W_x and the half spacing S_x are limited to 200 nm and 50 nm due to the EBL writing resolutions. For the comparison, the actually fabrication sizes and associated errors are also listed. The associated simulated reflectance $|S_{11}|$ curves and maximum overlap integral values I for different MQW thicknesses are shown in Fig. 13.

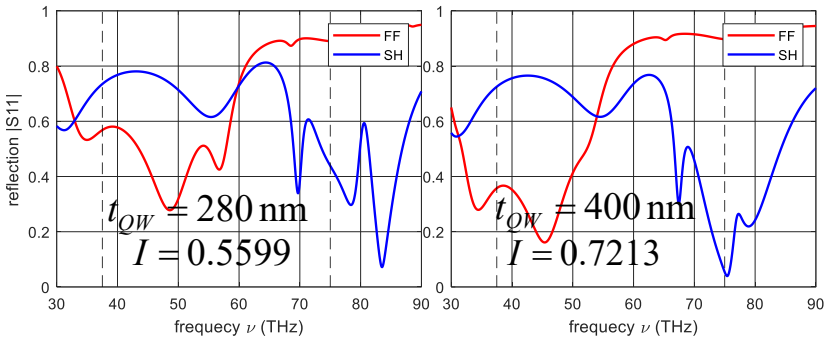

Fig. 13. Simulated reflectance $|S_{11}|$ of single nanoresonator of the incomplete back plane GaN SHG metasurface assuming the electric field of incident light is along x-axis (red lines) and y-axis (blue lines). The MQW thickness 280 and 400 nm, which are corresponding to 35 period and 50 period GaN MQW sample. The sizes of each nanoresonator are optimized (listed in Table 3) to achieve maximum overlap integral I, whose values are also listed aside the curves.

The fabrication steps of such incomplete back plane GaN SHG metasurface are described in Fig. 14. Each wafer was coated 400 nm silicon nitride (Si_3N_4) in plasma-enhanced chemical vapor deposition (PECVD). The Si_3N_4 layer was used to act as the hard mask in the inductively coupled plasma (ICP) etching. To do so, a positive electronic beam lithography (EBL) was used to define the T-shape antenna array and reactive ion etching (RIE) was used to transfer the patterns from EBL resistor to the Si_3N_4 layer. After the MQW dry etching in ICP and Si_3N_4 layer removal, a vertical 5 nm titanium (Ti) (to increase the adhesion) and 40 nm gold (Au) layers

were deposited to create the top antenna array and bottom incomplete back plane, so these two metal layers have same thickness.

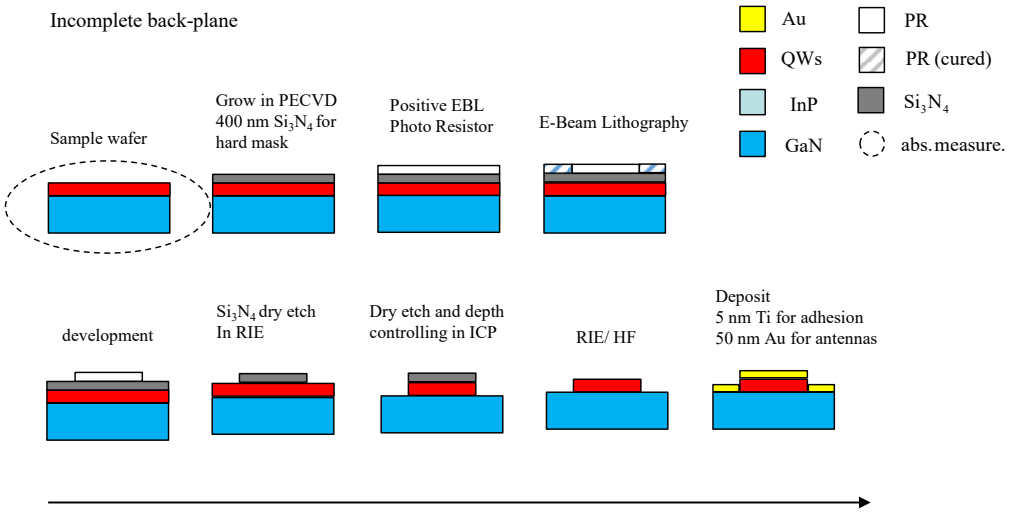

Fig. 14: Fabrication flow chart of incomplete back plane GaN SHG metasurface. A 400 nm Si_3N_4 layer is grown on the epi-side of MQW and patterned by an EBL to serve as the hard mask for the dry etching process. After removing Si_3N_4, a vertical Ti and Au layer were deposited to create the top antenna array and bottom incomplete back plane.

Figure 15 shows the SEM images of the fabricated incomplete back plane GaN SHG metasurface at two crucial steps. All fabrication errors are < 5%.

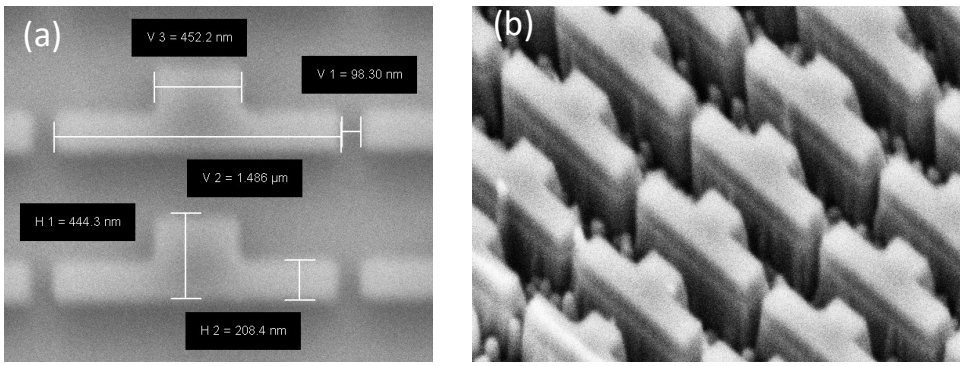

Fig. 15: SEM images of the fabricated incomplete back plane GaN SHG metasurface **(a)** after EBL and transferring pattern to Si_3N_4 hard mask and **(b)** after ICP dry etching but before the Si_3N_4 layer removal and the final metal deposition. The actual sizes were measured and listed in Table 3.

Despite successful metasurface processing from GaN/AlGaN heterostructures, no SHG was recorded. This is likely due to the level 3 in the designed ISB system to be in the intended position and/or not being optically coupled to state 1 as expected by theory, cf. Fig. 11.

3. Future work/work in progress

With the obtained strong ISB absorption peaks on r-plane sapphire, we have a number of steps initiated and will be continued in the next year, including

- Design, growth, and characterization of GaN-based multi-quantum-well (MQW) heterostructures with giant intersubband nonlinear response for second harmonic generation (SHG).
- Fabrication of metasurfaces with arrays of MQW-filled metal nanoresonators for SHG.

4. References

[1] M. Monavarian, J. Xu, m. Khoury, F. Wu, P. De Mierry, P. Vennegues, M.A. Belkin, and J.S. Speck, "Defect tolerance of intersubband transitions in nonpolar GaN/AlGaN heterostructures: A path toward low-cost and scalable mid- to far-infrared optoelectronics," *under review* (2021).

[2] N. Nookala, J. Xu, O. Wolf, S. March, R. Sarma, S. Bank, J. Klem, I. Brener, and M. A. Belkin, "Mid-infrared second-harmonic generation in ultra-thin plasmonic metasurfaces without a full-metal backplane," *Appl. Phys. B.* **124,** 132 (2018).

[3] J. Lee, M. Tymchenko, C. Argyropoulos, P.-Y. Chen, F. Lu, F. Demmerle, G. Boehm, M.-C. Amann, A. Alu, and M.A. Belkin, "Giant nonlinear response from plasmonic metasurfaces coupled to intersubband transitions," *Nature* **511,** 65–69 (2014).